encountered during grinding, and their high grinding resistance relative to the weaker rock matrix caused the RAT to stop operations (Plate 8). One spherule was slightly rotated during the grinding, and an irregular clast was plucked from the rock and thrown downhill during grinding. The estimated grinding energies for the rock targets at Meridiani Planum are relatively low, as compared to rocks at Gusev crater and most samples ground in the laboratory (Table 1). The grind energy correlates with the slope angles for the outcrop, in that the more resistant Guadalupe target ground by the RAT is located on a 36 ± 5° slope, whereas the less resistant McKittrick target is located on a 6.7 ± 2° slope. The higher slope for the Guadalupe outcrop is interpreted to be due to higher resistance to weathering than the McKittrick outcrop. Finally, even Bounce rock is weaker than rocks ground at Gusev crater, consistent with the densely fractured appearance of this rock (Plate 12). Bounce rock is an isolated target on the plains and was probably transported to its current location as impact ejecta (*12*). The fractures may have been introduced during ejection and impact of this rock.

The hematite-bearing plains that Opportunity landed on are at the top of a section of layered strata that is ~300 m thick and that disconformably overlies the Noachian-aged cratered terrain (*11*). We interpret the smooth, flat nature of Meridiani Planum to be due to differential stripping of horizontally layered strata, combined with continuing diffusion-driven mobilization of loose material to fill local depressions; i.e., soil fills in the craters, hollows, and troughs. Spherules, irregular particles, coarse sand covers, and basaltic soils represent the net result of concentration of these particles as the spherules were eroded from the weak evaporitic rocks in former and current aeolian environments. The hematite signature observed from orbit (*20*) that led us to land Opportunity in Meridiani Planum is due to a concentration of hematite-rich spherules that occurred as they were eroded from the evaporitic rocks. The lack of evaporite deposits in the soils on Meridiani Planum is due to relatively rapid aeolian erosion and removal as dust in suspension of these mechanically weak deposits. The amount of erosion is not well constrained, but it could range from meters to many meters.

References and Notes

1. S. W. Squyres *et al.*, *J. Geophys. Res.* **108**, 8062 (2003).
2. R. E. Arvidson *et al.*, *J. Geophys. Res.* **108**, 8070 (2003).
3. R. Li *et al.*, *J. Geophys. Res.* **107**, 8005 (2002).
4. Names have been assigned to areographic features by the Mars Exploration Rover (MER) Team for planning and operations purposes. The names are not formally recognized by the International Astronomical Union.
5. M. P. Golombek *et al.*, *J. Geophys. Res.* **108**, 8072 (2003).
6. A martian solar day has a mean period of 24 hours 39 min 35.244 s and is referred to as a sol to distinguish this from a roughly 3% shorter solar day on Earth.
7. The term martian soil is used here to denote any unconsolidated materials that can be distinguished from rocks, bedrock, or strongly cohesive sediment. No implication of the presence or absence of organic materials or living matter is intended.
8. G. A. Neumann *et al.*, *Geophys. Res. Lett.* **30**, 1561 (2003).
9. J. F. Bell III *et al.*, *Science* **306**, 1703 (2004).
10. R. E. Arvidson *et al.*, *Science* **305**, 5685 (2004).
11. R. E. Arvidson *et al.*, *J. Geophys. Res.* **108**, 8073 (2003).
12. P. R. Christensen *et al.*, *Science* **306**, 1733 (2004).
13. L. A. Soderblom *et al.*, *Science* **306**, 1723 (2004).
14. K. E. Herkenhoff *et al.*, *Science* **306**, 1727 (2004).
15. G. Klingelhöfer *et al.*, *Science* **306**, 1740 (2004).
16. S. W. Squyres *et al.*, *Science* **306**, 1698 (2004).
17. L. Richter, P. Hamacher, paper presented at the 13th Conference of the International Society for Terrain-Vehicle Systems, Munich, 14 to 19 September 1999.
18. S. P. Gorevan *et al.*, *J. Geophys. Res.* **108**, 8068 (2003).
19. T. M. Mynck *et al.*, paper 2004-6096 presented at the American Institute of Aeronautics and Astronautics (AIAA) Space 2004 Conference and Exhibit, San Diego, CA, 28 to 30 September 2004.
20. T. M. Christensen *et al.*, *J. Geophys. Res.* **105**, 9623 (2000).

21. We thank the MER Team and the scientists and engineers who made the landing, traverses, and science observations a reality. Work funded by NASA through the MER Project.

Plates Referenced in Article
www.sciencemag.org/cgi/content/full/306/5702/1727/DC1
Plates 8 and 12

18 August 2004; accepted 13 October 2004

RESEARCH ARTICLE

Mineralogy at Meridiani Planum from the Mini-TES Experiment on the Opportunity Rover

P. R. Christensen,[1]* M. B. Wyatt,[1] T. D. Glotch,[1] A. D. Rogers,[1] S. Anwar,[1] R. E. Arvidson,[2] J. L. Bandfield,[1] D. L. Blaney,[3] C. Budney,[3] W. M. Calvin,[4] A. Fallacaro,[4] R. L. Fergason,[1] N. Gorelick,[1] T. G. Graff,[1] V. E. Hamilton,[5] A. G. Hayes,[6] J. R. Johnson,[7] A. T. Knudson,[1] H. Y. McSween Jr.,[8] G. L. Mehall,[1] L. K. Mehall,[1] J. E. Moersch,[8] R. V. Morris,[9] M. D. Smith,[10] S. W. Squyres,[6] S. W. Ruff,[1] M. J. Wolff[11]

The Miniature Thermal Emission Spectrometer (Mini-TES) on Opportunity investigated the mineral abundances and compositions of outcrops, rocks, and soils at Meridiani Planum. Coarse crystalline hematite and olivine-rich basaltic sands were observed as predicted from orbital TES spectroscopy. Outcrops of aqueous origin are composed of 15 to 35% by volume magnesium and calcium sulfates [a high-silica component modeled as a combination of glass, feldspar, and sheet silicates (~20 to 30%)], and hematite; only minor jarosite is identified in Mini-TES spectra. Mini-TES spectra show only a hematite signature in the millimeter-sized spherules. Basaltic materials have more plagioclase than pyroxene, contain olivine, and are similar in inferred mineral composition to basalt mapped from orbit. Bounce rock is dominated by clinopyroxene and is close in inferred mineral composition to the basaltic martian meteorites. Bright wind streak material matches global dust. Waterlain rocks covered by unaltered basaltic sands suggest a change from an aqueous environment to one dominated by physical weathering.

The Mini-TES has provided remote measurements of mineral abundances and compositions, thermophysical properties, atmospheric temperature profiles, and atmospheric dust and ice opacities at the Opportunity rover landing site in Meridiani Planum. Mini-TES is a Michelson interferometer that collects infrared spectra from 5 to 29 μm (339 to 1997 cm^{-1}) at a spectral sampling of 10.0 cm^{-1} (*1–3*). Mini-TES observations of varying raster size and dwell lengths were acquired during rover operations within Eagle crater and during the traverse across the plains between Eagle and Endurance craters (*4*, *5*). Coregistered panoramic camera (Pancam) observations (*6*) provide context and additional multispectral visible and near-infrared observations. Reflected downwelling atmospheric radiance has been removed from all spectra presented here with the use of Mini-TES sky observations to directly measure the atmospheric radiance (*7*, *8*).

Mg and Ca sulfate–rich outcrops. Among the most exciting discoveries at Meridiani is the occurrence of bedrock with high

Table 1. Numerical deconvolution results for Mini-TES outcrop spectra. The volume abundances listed have been rounded to the nearest 5% from the values from the deconvolution model.

Mineral group	Guadalupe	Gills	Last Chance Lower	Last Chance Left	Hippo	Pilbara	Tamanend Park	Chantry Flats	Tres Creek	Rhino Horn	Bunny Slope	Dolphin	Hamersley
Sulfate	25	25	10	15	25	30	35	30	35	30	25	25	15
Hematite	25	25	0	20	35	0	35	30	45	45	10	40	5
Sheet silicate	0	0	0	0	0	0	10	20	0	0	0	5	0
Glass	25	15	15	20	10	20	10	10	5	5	20	15	20
Oxide/hyroxide	0	5	20	20	5	10	0	0	5	5	5	0	0
Feldspar	10	15	25	10	15	20	0	0	0	5	15	0	45
Olivine	10	10	20	10	5	10	10	10	5	10	15	5	0
Pyroxene	5	5	10	5	5	5	0	5	0	5	15	5	15
Total	100	100	100	100	100	95	100	105	95	105	105	95	100

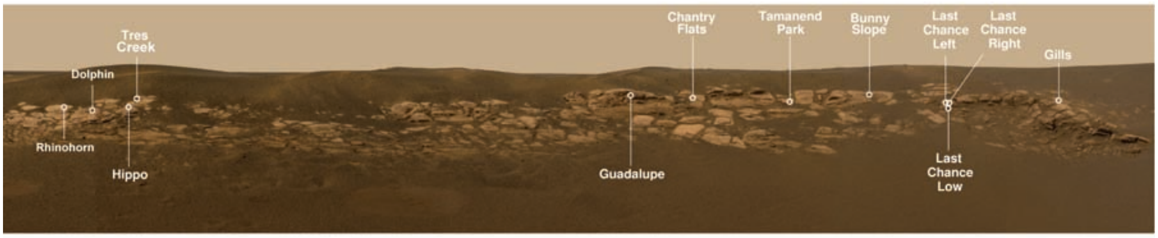

Fig. 1. Index map acquired from the lander showing the locations of the Mini-TES spectra of rocks within Eagle crater. The image is a mosaic 11.8 m in length made from Pancam images P2211, P2217, and P2218 acquired on sol 2.

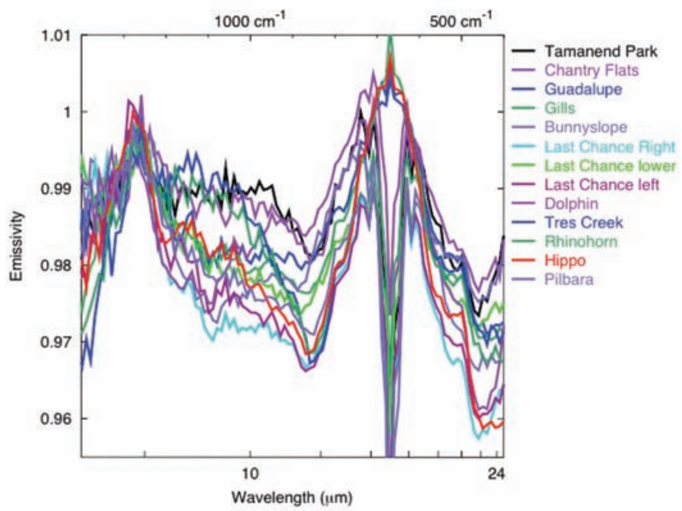

Fig. 2. Original Mini-TES spectra of the 13 outcrop locations. Variations in surface dust component and hematite spherules produce much of the variation in spectral character. All spectra presented here have been corrected to remove the effects of downwelling atmospheric radiance (*8*). Pilbara is located in Fram crater.

sulfur abundances and preserved sedimentary structures (*4*, *9*). Mini-TES spectra were acquired in long-integration single-point stares at 14 locations along the outcrops at Eagle and other craters (Figs. 1 and 2). These spectra have varying amounts of a surface dust component (*3*, *10*), which was removed by first deconvolving each spectrum with an endmember library of 47 laboratory minerals and four scene spectra (Fig. 3) (*11*–*15*) and then subtracting the derived dust component to produce a dust-free spectrum (Fig. 4). Once dust has been removed, the resulting spectra still have subtle differences in shape and derived mineral abundances, but all spectra show (i) a pronounced absorption beginning at ~1250 cm^{-1}, (ii) a relatively flat shape between 900 and 1200 cm^{-1}, (iii) an absorption shoulder at ~780 cm^{-1}, and (iv) deep absorptions near 450 and 550 cm^{-1} (Fig. 4). The absorption edge at 1250 cm^{-1} is consistent with the sulfate mineral group. The broad mid-wavelength absorption is fit by a mixture of glass, silicates, and sulfates. The long wavelength absorptions coincide with coarsely crystalline hematite (Fig. 3).

Sulfates are present in all of the outcrops we observed, with volume abundances, normalized to remove airfall dust, of 15 to 35% (Table 1) (*16*). The spectral library used to deconvolve the samples contained representative hydrous and anhydrous sulfates, including gypsum [$CaSO_4$-2(H_2O)], bassanite [2$CaSO_4$-(H_2O)], epsomite [$MgSO_4$-7(H_2O)], kieserite ($MgSO_4$-H_2O), glauberite [$Na_2Ca(SO_4)_2$], and jarosite [$KFe_3(SO_4)$-2$(OH)_6$] species. The best fit to the Mini-TES spectra was consistently provided by the Mg and Ca sulfates.

Jarosite, the Fe-bearing sulfate that was identified by the Mössbauer spectrometer (*17*), was detected in deconvolutions of several Mini-TES outcrop spectra but never in concentrations >5%. The outcrop has 17 weight % (wt %) FeO (*9*), with 28% of this Fe as jarosite (*17*). Together, these data indicate that ~10 wt % of the outcrop is jarosite. The average density of the outcrop derived with the Mini-TES mineral abundances (~3.3 g cm^{-3}; Table 1) is similar to the density of jarosite (3.1 to 3.3 g cm^{-3}),

[1]Department of Geological Sciences, Arizona State University, Tempe, AZ 85287, USA. [2]Department of Earth and Planetary Sciences, Washington University, St. Louis, MO 63130, USA. [3]Jet Propulsion Laboratory, California Institute of Technology, Pasadena, CA 91109, USA. [4]Department of Geological Science, Reno, NV 89557, USA. [5]Institute of Geophysics and Planetology, University of Hawaii, Honolulu, HI 96822, USA. [6]Department of Astronomy, Space Sciences Building, Cornell University, Ithaca, NY 14853, USA. [7]U.S. Geological Survey, Flagstaff, AZ 86001, USA. [8]Department of Earth and Planetary Sciences, University of Tennessee, Knoxville, TN 37996, USA. [9]National Aeronautics and Space Administration (NASA) Johnson Space Center, Houston, TX 77058, USA. [10]NASA Goddard Space Flight Center, Greenbelt, MD 20771, USA. [11]Space Science Institute, Martinez, GA 30907, USA.

*To whom correspondence should be addressed. E-mail: phil.christensen@asu.edu

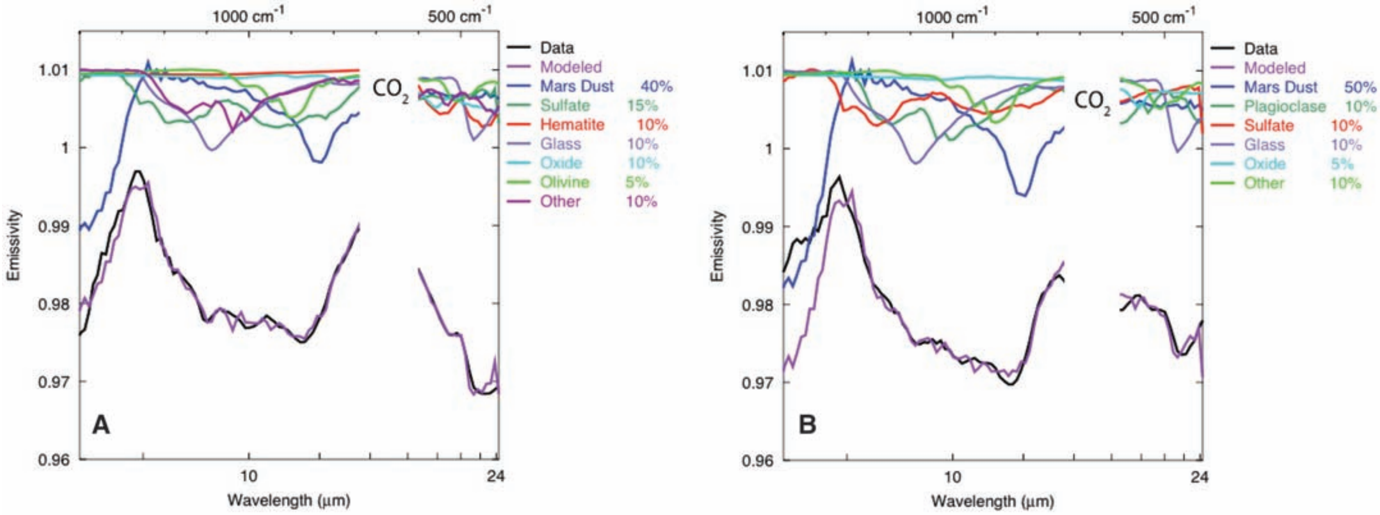

Fig. 3. (**A**) Spectral deconvolution of the Mini-TES spectrum of the outcrop at Gills in Eagle crater. The Mars dust component is subtracted from all of the measured spectra shown in Fig. 2 to produce the dust-removed spectra shown in Fig. 4. The individual minerals that fit to the spectra have been summed into mineral groups. The mineral abundances shown are best-fit values from the linear least squares deconvolution model; the endmember spectra are shown scaled by these abundances to show how each contributes to the measured spectrum. Derived abundances have accuracies of ±5 to 10%. Abundances shown in all figures have been rounded to the nearest 5%. Spectrum is average of 200 spectra acquired on sol 39. (**B**) Spectral deconvolution of the Mini-TES spectrum of the outcrop at Pilbara in Fram crater. The oxide component includes all oxides, typically modeled as magnetite and goethite, except hematite. Spectrum is the average of 100 spectra acquired on sol 85.

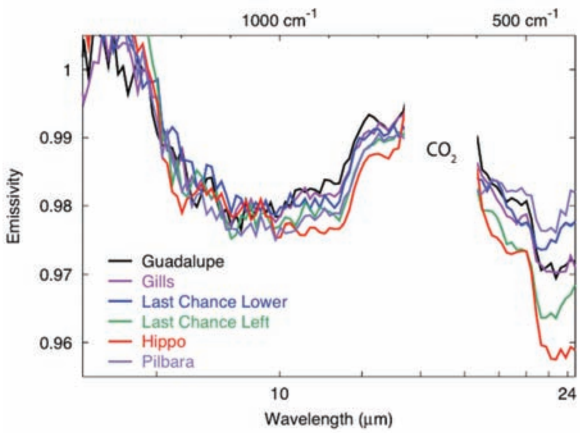

Fig. 4. Selected dust-removed spectra from outcrops in Eagle crater at locations Guadalupe, Gills, Last Chance Lower, Last Chance Left, and Hippo, and Fram crater at Pilbara. The spectrum of Pilbara is similar to the Eagle crater samples, suggesting that this rock is part of the same rock unit.

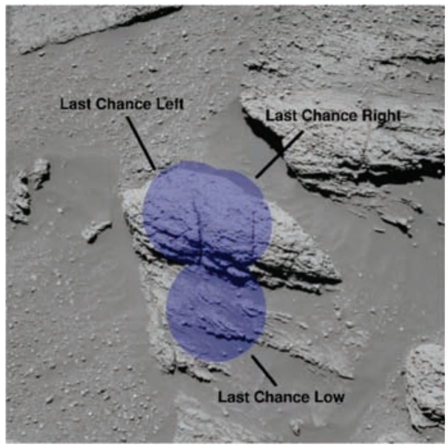

Fig. 5. Location of Mini-TES spectra for Last Chance outcrop location showing the mixture of outcrop, sand, and spherules that are present in the Mini-TES field of view. Each circle represents the Mini-TES field of view, which is ~15 cm in diameter.

indicating that the jarosite volume abundance is also ~10%. Given the low spectral contrast of this outcrop, this value is consistent with the marginal detection of jarosite by Mini-TES. The finding that Mg and Ca sulfates dominate is consistent with the Alpha Particle X-ray Spectrometer (APXS) results, which show that Mg and Ca are present, and that there is substantially more S and too little Fe for the sulfates to be jarosite alone (*9*, *18*).

Hematite is detected at volume abundances >10% in all but three outcrop locations (Table 1). Basaltic minerals are detected in all spectra. Loose, dark-toned sands and spherules that are likely wind transported from the overlying plains are common in cracks and ledges on the outcrop (Fig. 5) (*6*). Given the presence of these materials and the 12- to 15-cm diameter of the Mini-TES field of view (*19*), most of the Mini-TES observations are likely contaminated by these wind-blown materials and overestimate the hematite and basalt components (pyroxene and olivine) actually present in the outcrop. However, samples with the lowest basalt component (5 to 10%) still have hematite abundances of >30%. This Mini-TES–derived hematite abundance is higher than the abundance determined from the Mössbauer and APXS Fe results for the outcrop (*9*, *17*). However, it is likely that the larger Mini-TES fields of view (Fig. 5) included loose hematite-rich spherules observed in the Microscopic Imager (MI) (*20*) and Pancam images in the surrounding soils (*6*) in addition to the outcrop matrix and embedded spherules.

The areas of outcrop named Guadalupe, Gills, Last Chance Lower, Last Chance Left, Hippo, and Pilbara have the deepest absorption bands and provide the best Mini-TES measurement of the outcrop composition (Fig. 4). The reduced spectral contrast in other samples is likely due to multiple complicating effects, including blackbody cavity and temperature difference effects resulting from millimeter-scale pits (*21*). Intermediate- to high-silica components, modeled as high-silica glasses and feldspar, are fit to these six samples at abundances of ~10 to 25% (Table 1) (*13*, *14*, *16*, *22*–*25*). The derived abundance of the mafic igneous phases (olivine and pyroxene) varies from ~10 to 30%, with some of this component likely due to draping wind-blown sands (*6*). The derived abundance of oxides and hydroxides other than crystalline hematite, typically modeled as magnetite with minor goethite, is 5 to 20%. Taking the average of these best six outcrop spectra and deconvolving gives dust-removed abundances of 25% sulfate, 20% hematite, 30% high-silica component, 20% igneous phases, and 5% oxides other than hematite.

Light-toned outcrop is exposed in the ~10-m-diameter Fram crater, which is located 450 m from Eagle crater (*4*, *6*). Mini-TES spectra obtained from a sample of this outcrop at Pilbara (Fig. 4 and Table 1) are similar in spectral shape and derived mineral abundances to the outcrops at Eagle crater, suggesting that the process that formed these rocks was relatively uniform over a lateral distance of at least 450 m.

Mini-TES observations have demonstrated that crystalline silica minerals, such as quartz and chert, and carbonate phases are not present in these outcrops at abundances >~5%. The low olivine and pyroxene abundances in these rocks indicate that either they did not form from basaltic material or alteration of pyroxene and olivine in a basaltic parent rock has been nearly complete. The exact mineral phase of the high-silica component has not yet been determined, but the presence of these phases is consistent with the bulk APXS chemistry for the outcrop (*9*, *18*). The low abundance of other oxides and hydroxides in all but two samples (Table 1) is consistent with the results from the Mössbauer (*17*) and indicates that hematite is the dominant oxide and hydroxide in this outcrop.

Hematite spherules. The presence of coarsely crystalline hematite exposed on the surface has been predicted from orbital TES data (*26*, *27*) and was confirmed in the Mission Success panorama acquired beginning on sol 3 (*28*). The Mini-TES spectral signature of hematite is associated with spherules 0.6 to 6 mm in diameter (*20*). Mini-TES vertical scans of the plains were acquired from the near field to the horizon. These observations show a systematic increase in the depth of the diagnostic 450 and 550 cm^{-1} hematite absorption bands with decreasing elevation angle (Fig. 6), and a corresponding decrease in the depth of the basalt and dust component in the 700- to 1200-cm^{-1} region. The spectral shape of the hematite bands does not vary with elevation angle (e, measured downward from the horizontal), indicating that viewing geometry does not affect the spectral character of the spherules up to elevation angles of ~5° (*29*). With an average diameter (d) of 3 mm for the hematite spherules and only ~0.1 to 0.2 mm for the intervening sand (*30*), the spacing (x) of spherules only needs to be $x \leq d/\tan(90 - e)$, or ~25 mm, on the flat plains for the spherules to dominate the observed emission. This spacing is consistent with typical spherule spacing observed for plains soils (*30*, *31*).

Differencing the spectra from the highest and lowest elevation angles effectively isolates the spherule component of the soil. This derived spectrum matches a laboratory hematite sample (Fig. 7A) (*32*), which indicates that the spherules are dominated by hematite. No other components, including silica, carbonates, sulfates, silicates, or other oxides, are detected in the derived Mini-TES spherule spectra at a total abundance for non-hematite components of 5 to 10%. Whereas Mini-TES only directly samples the outermost 50 to 100 μm of the spherules (*33*), many of the spherules are eroded or broken (*30*), suggesting that the interiors of these particles are also dominated by hematite.

We tried to determine the spherule composition with the use of the entire instrument suite by comparing the hematite-rich Berry Bowl and nearby hematite-poor outcrop surfaces. However, the Mini-TES difference spectrum (Fig. 7B) shows the presence of hematite and basaltic sand, and Pancam images show the presence of dark-toned sand and spherules in the Berry Bowl (Plate 11) (*6*). This experiment demonstrates that the spectral differencing technique identifies all of the components that differ between the two observations, and provides support for the hematite-dominated spherule composition derived from the plains emission angle experiment.

The lateral distribution of hematite within Eagle crater was mapped by deconvolving high-resolution Mini-TES rasters acquired during the crater traverse to obtain mineral abundances (Plate 3). Hematite spherules occur nonuniformly around Eagle crater, with the highest abundance occurring on the western inner wall and decreasing on the northern wall (Plate 3). The crater floor has a low-hematite spectral signature over much of its surface. The trend of decreasing hematite abundance from the surrounding plains, along troughs and cracks in the outcrop, and onto the crater floor (Plate 3), suggests that these troughs are pathways of hematite transport from the plains into the crater. Thus, the primary source of hematite within the crater appears to be from the overlying plains, rather than from erosion of spherules present in the outcrop exposed in the crater wall.

The vertical distribution of hematite within the soils was investigated by comparing Mini-TES spectra of soils within and adjacent to

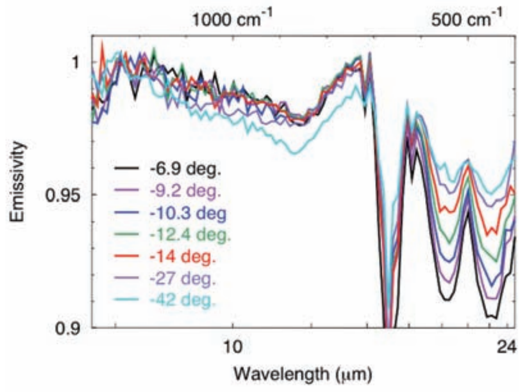

Fig. 6. Spectra of the plains surrounding Eagle crater at a range of elevation angles. The spectral bands at 450 and 550 cm^{-1}, where hematite has strong absorptions, deepen with decreasing elevation angle, corresponding to increasing emission angle. The basalt and dust silicate absorptions in the 750- to 1200-cm^{-1} region show a corresponding decrease, consistent with a reduction in basalt and an increase in hematite-rich spherules within the field of view at high emission angles. The deep absorptions centered near 667 cm^{-1} are due to atmospheric CO_2. Spectra were acquired on sol 72.

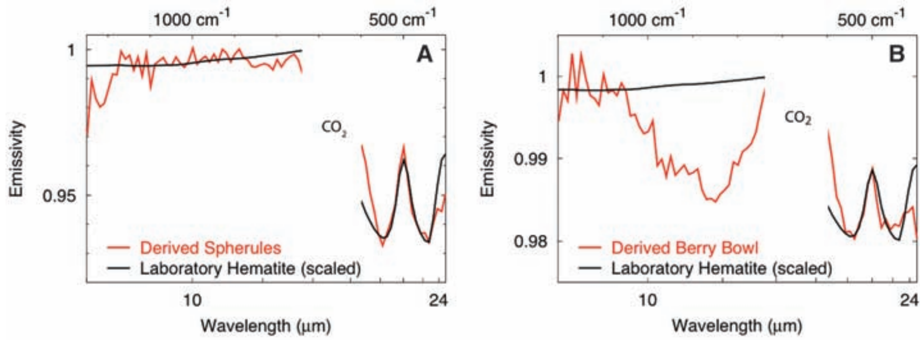

Fig. 7. (**A**) Derived Mini-TES spectra of spherules isolated by subtracting the high emission angle observation from the low emission angle observation shown in Fig. 6. The resulting spectrum matches a laboratory hematite sample (*32*). No other components are detectable in the derived Mini-TES spectrum, indicating that the spherules are dominated by hematite. (**B**) Derived spectrum of spherules and basalt sand within the Berry Bowl (*6*) determined by differencing a spectrum of the Berry Bowl from a spectrum from a nearby surface with low spherule and sand abundance. The derived Mini-TES spectrum is consistent with a mixture of hematite spherules (400 to 600 cm^{-1}) and basalt sand (750 to 1050 cm^{-1}), indicating that this differencing technique is sensitive to all components that were in the sample.

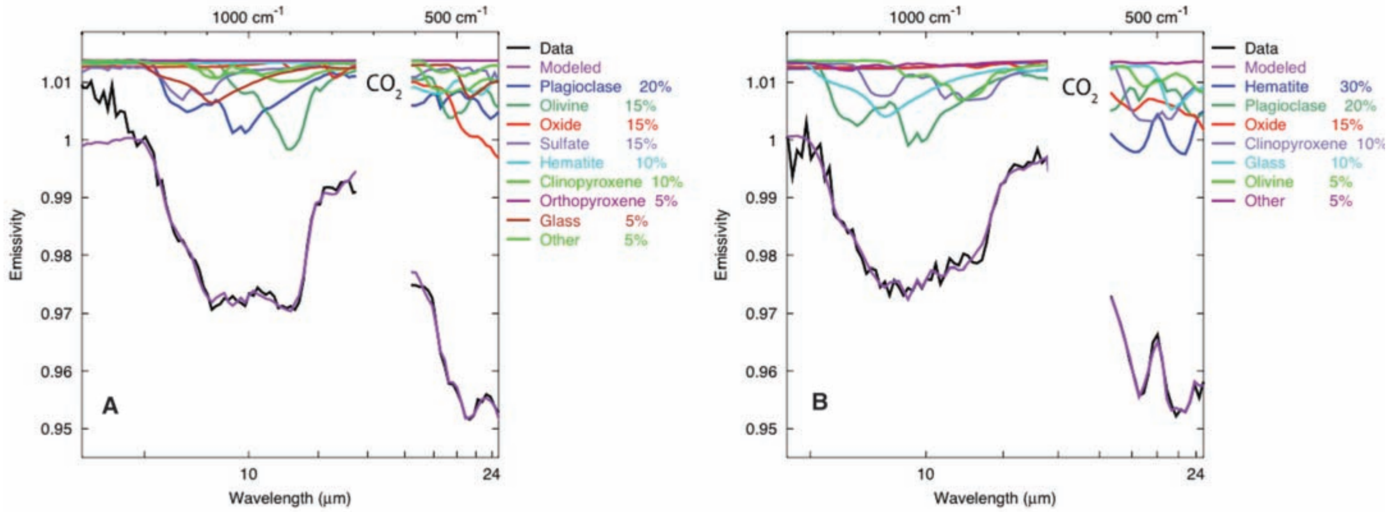

Fig. 8. (**A**) The mineral composition and abundance of basaltic sands on the floor of Eagle crater as derived from the deconvolution of dust-removed Mini-TES spectra. These sands are derived from a plagioclase, pyroxene, and olivine basalt with hematite and sulfate contaminants from the Eagle crater outcrop. Oxide includes all oxides except hematite. Spectrum is the average of 225 spectra acquired on sol 8. (**B**) The mineral composition and abundance of basalt and hematite spherule sands on the plains between Fram and Endurance craters derived from the deconvolution of dust-removed Mini-TES spectra. These sands appear to be derived from a plagioclase, pyroxene, and olivine basalt with more hematite and fewer sulfate contaminants than in the sands inside Eagle crater. Oxide component includes all oxides except hematite. Spectrum is the average of 90 spectra acquired on sol 90.

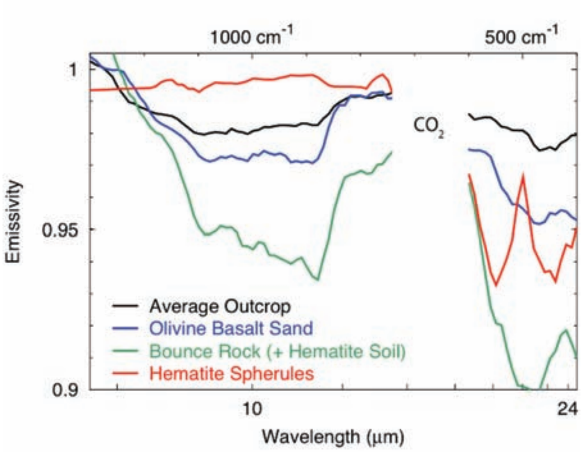

Fig. 9. Comparison of the spectral properties of the major components observed at the Meridiani landing site. The outcrop spectrum is the average of spectra of Guadalupe, Gills, Last Chance Lower, Last Chance Left, Hippo, and Pilbara; the olivine basalt sand spectrum is from Fig. 8A; the Bounce rock spectrum is from Fig. 10A; the hematite spherule spectrum is from Fig. 7A.

airbag bounce marks (*4*, *30*). The undisturbed soils show hematite absorptions at 450 and 550 cm^{-1} that are due to hematite spherules on the surface. The depths of these spectral bands are reduced in the spectra from bounce marks, indicating that the surficial hematite spherules were pushed beneath the surface by the airbag impact. MI observations support this by showing spherules pushed beneath the surface by placement of the Mössbauer instrument (*20*). These observations suggest that the spherules are a surficial lag, with a lower concentration in the subsurface fine-grained materials. This interpretation is supported by observations of vertical walls produced in trenching activities that show few spherules exposed in the trench walls (*30*, *34*). A possible scenario for the formation of this lag and the higher hematite spherule abundance on the plains is the erosion of an overlying spherule-bearing layer.

Olivine basalt soils. Soils with low hematite abundance all have similar mineralogies and are composed of basaltic minerals plagioclase, high-Ca clinopyroxene, olivine [~Fo60 (*35*)], oxides, orthopyroxene, and glass (Fig. 8). The sands on the floor of Eagle crater have derived mineral abundances, normalized to remove the dust, hematite, and sulfate components, of more intermediate plagioclase (~30%) than pyroxene (~20%), with ~20% olivine (~Fo60), ~10% glass, and ~15% oxides other than hematite, which are typically modeled as magnetite and lesser goethite (Fig. 8A). The sands on the plains between Eagle and Endurance craters typically have higher hematite abundance (Fig. 8B), but when these spectra are normalized to remove the dust, hematite, and sulfate components, they are also dominated by intermediate plagioclase (~35%), with 15% clinopyroxene, 10% ~Fo60 olivine, 15% glass, and 20% other oxides (Fig. 8B). Overall, these sands have a higher abundance of plagioclase relative to pyroxene and are close to the mineral compositions and abundances derived from orbital TES data for typical martian basaltic units found in the ancient cratered terrains of Mars (*23*, *24*, *36*).

These olivine basalt sands are not derived from any rock observed to date at Meridiani. It is possible that the sands at this site were transported from outside the layered terrain of Meridiani. However, the distance that a 500-μm basalt grain can be transported by aeolian saltation before it is reduced to a size that can be carried off in suspension is only ~300 km (*37*, *38*). Alternatively, these sands may have been derived from the mechanical breakdown of an overlying layer or from underlying material brought to the surface by impact cratering. The variability in olivine abundance may be due to transport sorting processes or may reflect real variations in the composition of source rocks that produced these sands.

Bounce rock. Bounce rock, the largest and darkest rock present on the exterior rim of Eagle crater, was selected for detailed investigation (*4*). The Mini-TES–derived mineral composition of Bounce rock, after the removal of airfall dust and the small amount of fine dust contaminant produced by the Rock Abrasion Tool (RAT) during abrasion of this rock, shows that Bounce rock is unique

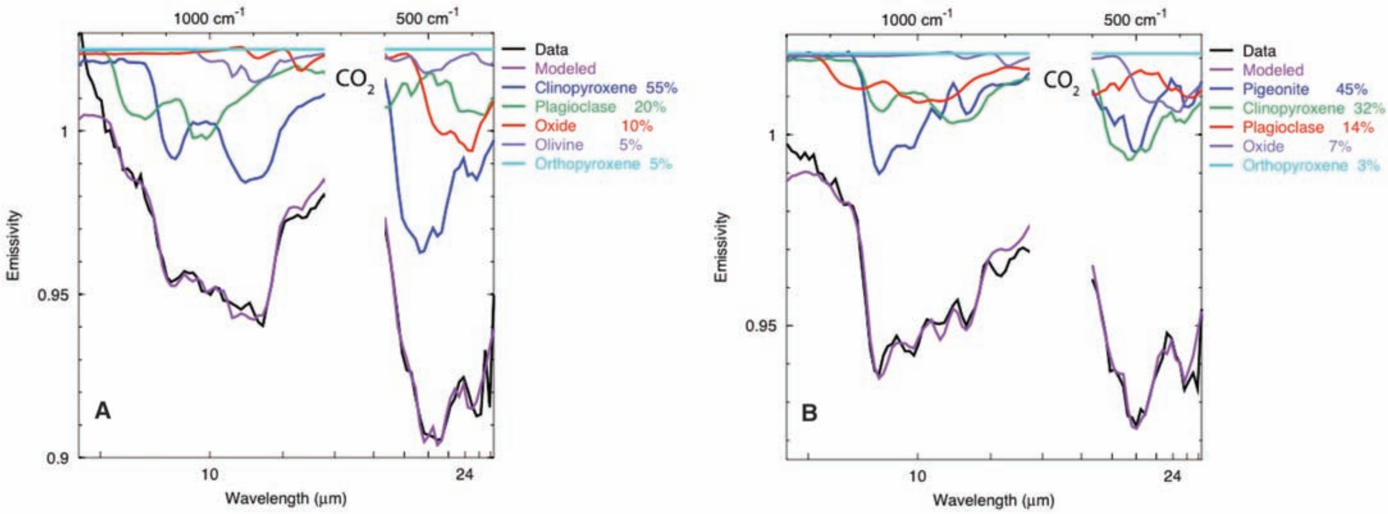

Fig. 10. (**A**) The mineral composition and abundance of Bounce rock as determined from the deconvolution of the average of 100 dust-removed Mini-TES spectra acquired on sol 68. This rock has much more clinopyroxene compared to plagioclase than seen in the basaltic sands. Oxide includes all oxides except hematite. Spectrum is the average of 100 spectra collected on sol 68. (**B**) The mineral composition of EETA#79001B from a laboratory spectrum (*41*). The spectrally derived composition of this rock matches its measured modal mineralogy (*43*). The spectrum of this meteorite differs from that of Bounce rock in the 9- to 12-μm region, suggesting that although the elemental abundance of Bounce rock matches that of EETA#79001B (*9*), the nature or composition of the pyroxenes may be somewhat different.

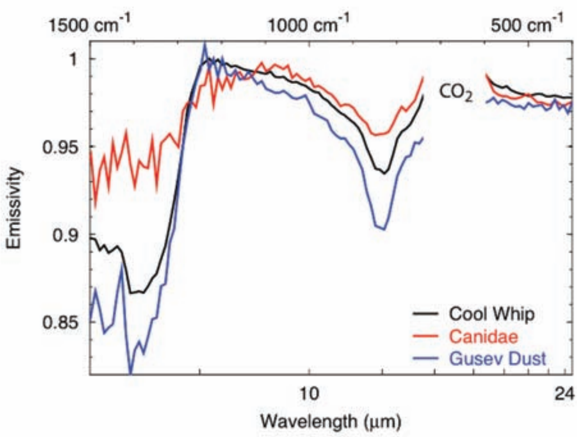

Fig. 11. The mineral composition and abundance of the bright material in soil and rocks. The surface at location Cool Whip is in the bright wind streak trending southeast from Eagle crater. This surface is essentially pure dust as determined from comparison with a dust spectrum from Gusev crater (*3*), suggesting formation from air-fall dust. Canidae is a bright, dust-covered rock on the rim of Endurance crater.

among rocks investigated at either the Meridiani or Gusev sites (Fig. 9) (*3*, *39*).

Bounce rock has much higher pyroxene abundance than the basaltic sands and rocks observed here and at Gusev crater (*3*, *39*), with clinopyroxene accounting for ~55% of the rock and orthopyroxene ~5%, followed by ~20% plagioclase, ~5% olivine, and ~10% oxides (Fig. 10A). This composition is much closer to that of the martian basaltic shergottite meteorites (*40*) than the basaltic components observed at either Mars Exploration Rover (MER) site.

The elemental abundance of Bounce rock is similar to that of EETA#79001 lithology B (*9*); however, the infrared spectra of EETA#79001B (Fig. 10B) (*41*, *42*) and Bounce rock differ in the 9- to 12-μm region. Deconvolution of the laboratory spectrum of EETA#79001B (Fig. 10B) gives mineral abundances that closely match its measured modal mineralogy of 30 to 50% pigeonite, 10 to 25% high-Ca clinopyroxene, ~30% maskelynite (shocked plagioclase), and 5% opaque minerals (*43*). The best fit to the Bounce rock spectrum (Fig. 10B) gives high-Ca clinopyroxene instead of the low-Ca clinopyroxene pigeonite, although the four emissivity minima between 850 and 1100 cm^{-1} suggest that pigeonite is present in Bounce rock but poorly modeled with our current collection of pigeonite samples.

The TES-derived basalt compositions differ from those of the martian meteorites (*24*, *44*, *45*), and both lithologies have now been positively identified in situ on Mars. The ability of Mini-TES spectra to distinguish them and the similarity of Meridiani spectra to the TES orbital spectra strengthens previous interpretations that use TES data to determine the composition of basalt globally (*23*, *24*, *36*, *44*).

The distinct mineral composition and chemistry of Bounce rock, together with its isolated occurrence (*4*), suggest that this rock may not be locally derived. A possible source region is a relatively unmodified 25-km crater located 75 km southwest of Eagle crater, the continuous ejecta of which lie atop the hematite-bearing plains (*4*, *27*). In this case, Bounce rock may have been derived from materials that are compositionally distinct from the basaltic sands that cover the plains around Eagle crater (*4*).

Hamersley rock in Fram crater. A rock called Hamersley observed on the inner wall of the ~10-m-diameter crater Fram has a derived mineral abundance and composition that may be another endmember among the samples observed to date. Hamersley has the highest abundance of high-silica components (modeled as glass, feldspar, and sheet silicate) observed, although Bunny Slope and Dolphin at Eagle crater have similar spectral shapes.

Dust accumulation: Eagle crater bright streak. Upon exiting Eagle crater, Opportunity examined the composition and texture of the bright material seen from orbit to form a wind streak oriented downwind from Eagle crater (*4*, *30*). Mini-TES spectra of the surface within this streak match the spectra of typical bright low-inertia dust seen globally from orbit (*46*) and in situ at Gusev crater (*3*) (Fig. 11). The spectral match between this wind streak and regional dust deposits provides support for the model of bright wind streaks forming by deposition of airborne dust in the stagnant air created downwind of topographic obstacles during periods of high atmospheric stability (*47*).

Dust accumulation occurs on all of the outcrop rocks to some degree (Fig. 2). On some rocks, such as Canidae observed on the rim of Endurance crater, dust accumulates to sufficient thickness (>~50 μm) (*48*, *49*) to mask the spectrum of the underlying rock (Fig. 11). Dust may accumulate more readily on rock surfaces than on the soil, because occasional saltation of sand-sized grains may entrain and remove the dust, resulting in surfaces that are dark and have a small dust component in Mini-TES spectra.

Global context. Analysis of orbital data has suggested that the extensive (500 × 250 km), ancient (*50*–*52*), layered, hematite-bearing units in Meridiani Planum formed by (i) chemical precipitation of a hematite precursor (*32*) from Fe-rich aqueous fluids under ambient conditions (*26*, *27*, *53*); (ii) precipitation from Fe-rich hydrothermal fluids (*26*, *27*, *51*, *54*); (iii) thermal oxidation of volcanic ash during eruption (*26*, *27*, *51*, *55*); or (iv) precipitation of Fe-oxides that were metamorphosed by burial to platy hematite (*56*).

These units were deposited in a standing body of liquid water on the basis of the morphology, composition, and vertical distribution of the hematite-bearing units seen from orbit (*53*). The discovery of sulfate-rich outcrops and hematite in concretions has provided conclusive evidence for deposition in an ancient aqueous system (*18*). However, the presence of extensive olivine, pyroxene, and feldspar in basaltic sands at this site and throughout Meridiani (*53*) suggests that physical weathering has dominated over chemical weathering during the time that these sands have been exposed on the surface. On a broader scale, the occurrence of basalts and olivine basalts throughout much of the equatorial and mid-latitude regions (*3*, *25*, *57*) suggests that chemical weathering may have been a relatively minor process, at least in low to mid-latitudes (*58*), throughout much of martian history. Thus, the presence of a body of water may represent a relatively brief, localized phenomenon early in Mars history.

References and Notes

1. P. R. Christensen *et al.*, *J. Geophys. Res.* **108**, 8064, 10.1029/2003JE002117 (2003).
2. Two-point radiometric calibration was intended to use two V-groove blackbody targets. However, as with the Spirit rover, the temperature sensors attached to the rover deck failed at extremely low temperatures (~–90°C) on the first night after landing. The calibration was modified to use prelaunch measurements of the instrument response function taken over temperature, with the instrument radiance determined from observations of the target mounted in the Pancam Mast Assembly. On the basis of comparison with orbiting Mars Global Surveyor (MGS) TES data and modeling of the atmospheric observations, the response function has not changed from prelaunch values and the calibration approach is providing the required accuracy. The 1σ radiometric precision for two-spectra summing is ±1.8 × 10^{-8} W cm^{-2} sr^{-1}/cm^{-1} between 450 and 1300 cm^{-1}, increasing to ~7 × 10^{-8} W cm^{-2} sr^{-1}/cm^{-1} at shorter (300 cm^{-1}) and longer (1800 cm^{-1}) wave numbers. The absolute radiance error is <5 × 10^{-8} W cm^{-2} sr^{-1}/cm^{-1}, decreasing to ~1 × 10^{-8} W cm^{-2} sr^{-1}/cm^{-1}.
3. P. R. Christensen *et al.*, *Science* **305**, 837 (2004).
4. S. W. Squyres *et al.*, *Science* **306**, 1698 (2004).
5. Names have been assigned to aerographic features by the MER team for planning and operations purposes. The names are not formally recognized by the International Astronomical Union.
6. J. F. Bell III *et al.*, *Science* **306**, 1703 (2004).
7. M. D. Smith *et al.*, *Science* **306**, 1750 (2004).
8. The downwelling radiance is removed by solving for ε in the equation: radiance = $B(T_{surface} \times \varepsilon_{surface}) + (R_{atmosphere} \times R_{surface})$, where radiance is the measured total radiance from the surface, B is the Planck function, $T_{surface}$ is the surface temperature, $\varepsilon_{surface}$ is the surface emissivity, $R_{atmosphere}$ is the downwelling atmospheric radiance, and $R_{surface}$ is the surface infrared reflectivity that is equal to $(1 - \varepsilon_{surface})$. The surface temperature is derived from the measured Mini-TES spectrum (*1*, *3*). $R_{atmosphere}$ is the hemispherically integrated downwelling from the atmosphere and is approximated with Mini-TES observations taken at an emission angle of 60° from the zenith. The spectral radiance of the atmospheric path between Mini-TES and the target is assumed to be negligible, and the atmospheric transmissivity in this path is assumed to be 1.0. Removing the downwelling radiance deepens the absorption bands (*1*), but given the relatively high surface temperatures (typically >265 K) and the relatively low atmospheric opacity, the effect of the atmosphere on the spectra presented here is relatively small; the derived mineral abundances typically vary by less than 5% for any mineral for deconvolutions done with and without an atmospheric correction. Calculations based on the Discrete Ordinate Radiative Transfer code and including emitted, absorbed, and scattered surface and atmospheric radiative terms support the above conclusions.
9. R. Rieder *et al.*, *Science* **306**, 1746 (2004).
10. "Dust" is used throughout to indicate the fine-grained component of surface materials with similar spectral character to regional dust deposits observed by MGS TES and interpreted to be air fallout from regional and global dust storms.
11. The mineral suite used for deconvolution included a broad range of sulfate, carbonate, sheet silicates, oxides, pyroxene, feldspar, olivine, and surface dust compositions.
12. J. B. Adams, M. O. Smith, P. E. Johnson, *J. Geophys. Res.* **91**, 8098 (1986).
13. M. S. Ramsey, P. R. Christensen, *J. Geophys. Res.* **103**, 577 (1998).
14. K. C. Feely, P. R. Christensen, *J. Geophys. Res.* **104**, 24195 (1999).
15. V. E. Hamilton, P. R. Christensen, *J. Geophys. Res.* **105**, 9717 (2000).
16. The Mini-TES–derived volume abundances are estimated to have accuracies of ±5 to 10% on the basis of similar analyses of laboratory and MGS TES rock and mineral mixtures. The abundances listed in the figures and tables are the numerical best fit values derived from the linear least squares deconvolution model and are reported at the precision determined from the deconvolution model.
17. G. Klingelhöfer *et al.*, *Science* **306**, 1740 (2004).
18. S. W. Squyres *et al.*, *Science* **306**, 1709 (2004).
19. The Mini-TES nominal field of view is 20 mrad at infinity. For near-field observations, the field of view is the aperture diameter (6.35 cm) plus the 20-mrad divergence from the location of the telescope to the point being observed. Targets in the arm work volume are ~1.5 m in front of the rover, giving a total path length of ~3 m from the Mini-TES telescope. The resulting Mini-TES field of view is ~12 cm at the end of the rover arm.
20. K. E. Herkenhoff *et al.*, *Science* **306**, 1727 (2004).
21. J. Ondrusek, P. R. Christensen, J. H. Fink, *J. Geophys. Res.* **98**, 15903 (1993).
22. M. B. Wyatt, V. E. Hamilton, J. H. Y. McSween, P. R. Christensen, L. A. Taylor, *J. Geophys. Res.* **106**, 14711 (2001).
23. V. E. Hamilton, M. B. Wyatt, J. McSween, *J. Geophys. Res.* **106**, 14733 (2001).
24. P. R. Christensen, J. L. Bandfield, M. D. Smith, R. N. Clark, *J. Geophys. Res.* **105**, 9609 (2000).
25. J. L. Bandfield, *J. Geophys. Res.* **107**, 10.1029/2001JE001510 (2002).
26. P. R. Christensen *et al.*, *J. Geophys. Res.* **105**, 9623 (2000).
27. P. R. Christensen, R. V. Morris, M. D. Lane, J. L. Bandfield, M. C. Malin, *J. Geophys. Res.* **106**, 23873 (2001).
28. A martian solar day has a mean period of 24 hours 39 min 35.244 s and is referred to as a sol to distinguish this from a roughly 3% shorter day on Earth.
29. The millimeter-sized spherules are substantially larger than the wavelength of the emitted radiance. In this case, emission from the spherules should not exhibit angle-dependent emission because of Fresnel effects, which would be expected for a specular surface composed of particles comparable in size to the wavelength measured.
30. L. A. Soderblom *et al.*, *Science* **306**, 1723 (2004).
31. The term martian soil is used here to denote any loose unconsolidated materials that can be distinguished from rocks, bedrock, or strongly cohesive sediments. No implication of the presence or absence of organic materials or living matter is intended.
32. T. D. Glotch, R. V. Morris, P. R. Christensen, T. G. Sharp, *J. Geophys. Res.* **109**, EO7003, 10.1029/2003JE002224 (2004).
33. P. R. Christensen, S. T. Harrison, *J. Geophys. Res.* **98**, 19819 (1993).
34. R. E. Arvidson *et al.*, *Science* **306**, 1730 (2004).
35. The Fo (forsterite) value is the amount of FeO in the olivine, where forsterite is the Mg endmember and fayalite is the Fe endmember.
36. J. L. Bandfield, V. E. Hamilton, P. R. Christensen, *Science* **287**, 1626 (2000).
37. R. Greeley, M. D. Kraft, *Lunar and Planet. Sci. XXXII*, CD-ROM (abstr. 1839) (2001).
38. D. Rogers, P. R. Christensen, *J. Geophys. Res.* **108**, 5030, 10.1029/2002JE001913 (2003).
39. H. Y. McSween Jr. *et al.*, *Science* **305**, 842 (2004).
40. H. Y. McSween Jr., *Meteoritics* **29**, 757 (1994).
41. J. L. Bishop, V. E. Hamilton, *64th Annual Meteoritical Society Meeting* **36**, 21 (abstr. 5217) (2001).
42. V. E. Hamilton, P. R. Christensen, H. Y. McSween Jr., *J. Geophys. Res.* **102**, 25593 (1997).
43. H. Y. McSween Jr., E. Jarosewich, *Geochim. Cosmochim. Acta* **47**, 1501 (1983).
44. H. Y. McSween Jr., T. L. Grove, W. B. Wyatt, *J. Geophys. Res.* **108**, 5135, 10.1029/2003JE002175 (2003).
45. V. E. Hamilton, P. R. Christensen, J. H. Y. McSween, J. L. Bandfield, *Meteor. Planet. Sci.* **38**, 871 (2003).
46. J. L. Bandfield, T. D. Glotch, P. R. Christensen, *Science* **301**, 1084 (2003).
47. J. Veverka, P. Gierasch, P. Thomas, *Icarus* **45**, 154 (1981).
48. J. R. Johnson, P. R. Christensen, P. G. Lucey, *J. Geophys. Res.* **107**, 10.1029/2000JE001405 (2002).
49. T. G. Graff, thesis, Arizona State University (2003).
50. B. M. Hynek, R. J. Phillips, *Geology* **29**, 407 (2001).
51. B. M. Hynek, R. E. Arvidson, R. J. Phillips, *J. Geophys. Res.* **107**, 5088, 10.1029/2002JE001891 (2002).
52. M. D. Lane, P. R. Christensen, W. K. Hartmann, *Geophys. Res. Lett.* **30**, 1770, 10.1029/2003GL017183 (2003).
53. P. R. Christensen, S. W. Ruff, *J. Geophys. Res.* **109**, EO8003, 10.1029/2003JE002233 (2004).
54. D. C. Catling, J. M. Moore, *Icarus* **165**, 277 (2003).
55. R. E. Arvidson *et al.*, *J. Geophys. Res.* **108**, 8073, 10.1029/2002JE001982 (2003).
56. M. D. Lane, R. V. Morris, S. A. Mertzman, P. R. Christensen, *J. Geophys. Res.* **107**, 5126, 10.1029/2001JE001832 (2002).
57. T. Hoefen *et al.*, *Science* **302**, 627 (2003).
58. M. B. Wyatt, *Geology* **32**, 645 (2004).

59. We thank all of the individuals at Raytheon Santa Barbara Remote Sensing, led by S. Silverman, and at the Jet Propulsion Lab, whose effort and dedication have led to the successful acquisition of Mini-TES data from the surface at Meridiani Planum. We thank J. Bishop for providing the spectrum of EET A79001B. A. Watson provided assistance with data processing analysis. Funding was provided by the MER Project Science Office.

Plates Referenced in Article

www.sciencemag.org/cgi/content/full/306/5702/1733/DC1

Plates 3 and 11

7 September 2004; accepted 3 November 2004

Mineralogy at Meridiani Planum from the Mini-TES Experiment on the Opportunity Rover
P. R. Christensen *et al.*
Science **306**, 1733 (2004);
DOI: 10.1126/science.1104909